Faculty and Researchers   Faculty and Researchers' Publications

2017

Dynamics and Control Challenges for Imaging Satellites

Agrawal, Brij N.; Kim, Jae Jun

American Astronautical Society (AAS)

American Astronautical Society

Third IAA Conference on
DYNAMICS AND CONTROL OF
SPACE SYSTEMS 2017

Volume 161
ADVANCES IN THE ASTRONAUTICAL SCIENCES

Edited by
Yury N. Razoumny
Filippo Graziani
Anna D. Guerman
Jean-Michel Contant

RUDN
university

Proceedings of the 3rd International Academy of Astronautics Conference on Dynamics and Control of Space Systems (DyCoSS) held May 30 – June 1, 2017, RUDN University, Moscow, Russia.

DYNAMICS AND CONTROL CHALLENGES FOR IMAGING SATELLITES

Brij N. Agrawal* and Jae Jun Kim†

Imaging satellites have several challenges in dynamics and control to meet high performance requirements. As an example, Hubble Space Telescope pointing requirements are of 0.012 arc-sec and jitter requirements not to exceed 0.007 arc-sec. These satellites require fast slew maneuver with minimum slew time. Flexibility/control interaction becomes critical for these satellites. These satellites require fine mirror surfaces for diffraction limited performance. For visible images, the surface mirror accuracy requirements are a minimum of 30 nm. In order to meet these performance requirements, advance dynamics and control techniques and actuators and sensors are required. Meeting these requirements becomes even more challenging for future imaging satellites as the diameter of primary mirrors increases, resulting in deployable mirrors. This paper provides an overview of advanced dynamics and control techniques for jitter control, flexibility/control interactions, slew maneuvers, and reflector active surface control.

INTRODUCTION

Imaging satellites have very high performance requirements for pointing, jitter, slew maneuvers, and primary mirror surface accuracy for diffraction limited image quality. These high performance requirements pose many challenges in dynamics and control design resulting in the use of advance dynamics and control techniques and high performance actuators and sensors. As an example, Figure 1 shows Hubble Space Telescope. Hubble Space Telescope (HST) was launched in April 1990 by Space Shuttle Discovery. Its orbit altitude is 600 km, with 28.5 degree inclination. Wavelength coverage is 110-1100 nm. The diameter of the primary mirror is 2.4 meters. Optical resolution is 0.043 arc-sec (0.00001 Deg.). It has 3-axis stabilized zero momentum control system using reaction wheels with pointing accuracy of 0.012 arc-sec (0.000003 degree). It has jitter and pointing stability requirements of 0.007 arc-sec. The HST had several problems with the performance. Shortly after the HST was deployed in 1990, the telescope's primary mirror was discovered to have a flaw called spherical aberration. The outer edge of the mirror was ground too flat by a depth of 2.2 micron. This aberration resulted in images that were fuzzy because some of the light from the objects being studied scattered. Fortunately, HST orbiting at 600 km was the first telescope designed to be visited in space by astronauts to perform repairs, replace parts, and update its technology with new instruments. On Servicing Mission 1, December 2-13, 1993, astronauts installed COSTAR, consisting of five pairs of corrective mirrors in front of the

---

* Distinguished Professor, Mechanical and Aerospace Engineering, Naval Postgraduate School, Monterey, California 93943, U.S.A.
† Research Associate Professor, Mechanical and Aerospace Engineering, Naval Postgraduate School, Monterey, California 93943, U.S.A.

camera to counteract the flawed shape of the mirror. There was a problem with achieving pointing accuracy due to solar array flexibility and control interactions. New solar array and several other sensors were also installed by the astronauts. The HST shows the challenges in meeting performance requirements of imaging satellites even with a $1.5 billion program.
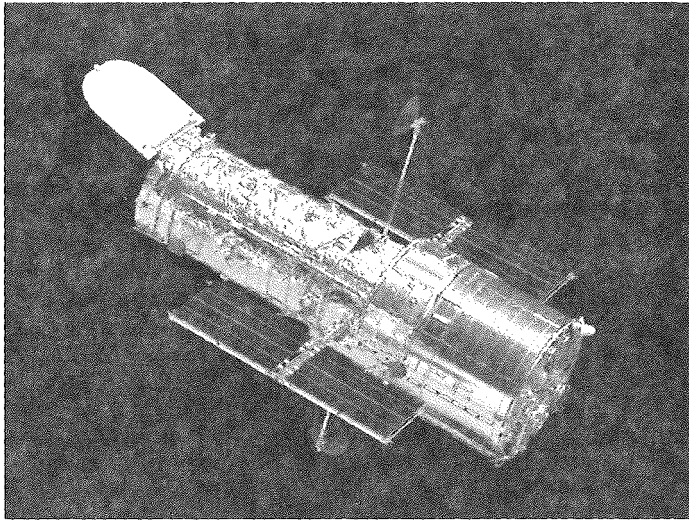

Figure 1. Hubble Space Telescope [1]

James Webb Space Telescope (JWST), the most challenging imaging satellite, is a 6.5 meter aperture observatory optimized for infrared astronomy (0.6-28 micron). JWST is shown in Figure 2. JWST is to be launched in orbit at L2 point at distance 1.5 million kilometers from Earth. Launch vehicle is Ariane 5. Optical resolution is 3 milliarcseconds (0.0000008 degree). The primary mirror consists of 18 hexagonal shaped mirror segments, each 1.32 meters in diameter. Each segment weighs approximately 20 Kg and is made out of beryllium, which is both strong and light. Compare to HST primary mirror whose mass density is 183 kg/m^2, it is 14.6 kg/m^2 for JWST. Each primary mirror segment is mounted on an actuator array that provides six degrees of freedom motion for phasing the segments and an additional radius of curvature adjustment actuator. Three segments on each side fold up during launch so that it can fit into the rocket. JWST has been a very challenging program for NASA. It was originally planned to be launched in 2011 with a budget of $1.6 billion and at this time; JWST is now planned to be launched in October 2018 with a budget of $8.8 billion.

The experiences on HST and JWST clearly show that imaging satellites with large aperture have very high challenging performance requirements and it is very challenging to meet these requirements. In the future, it is desired for imaging satellites to have deployable aperture in the range of 10-15 meters diameter. For these satellites, meeting performance requirements will be even more challenging requiring developments of advanced techniques and sensors and actuators in several areas of dynamics and control. This paper in the following sections provides an overview of advanced dynamics and control techniques for jitter control, flexibility/control interactions, slew maneuvers, and reflector active surface control.
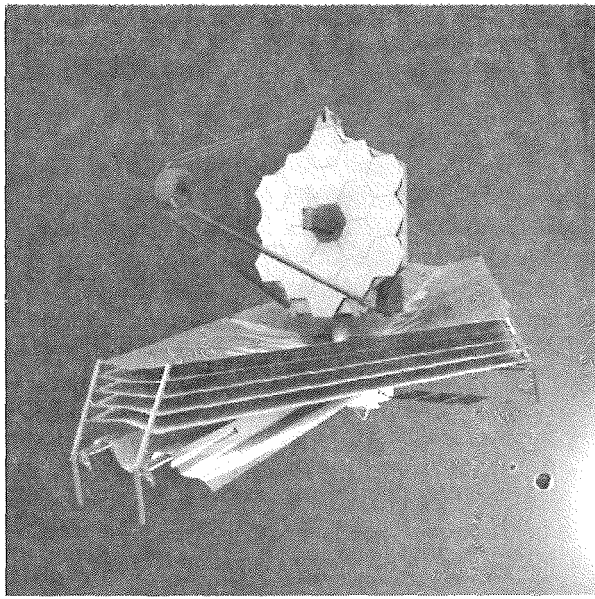
Figure 2. James Webb Space Telescope [2]

JITTER CONTROL

As we discussed earlier, imaging satellites require very tight jitter control. As an example, the requirement for HST is 0.007 arc-sec. In order to achieve these requirements, passive jitter control techniques are first considered. However, if the passive methods cannot achieve the desired jitter performance, the active jitter control of the optical beam will need to be implemented by using a fast steering mirror.

Figure 3. Vibration Control Techniques [3]

Figure 3 shows different techniques for reducing jitter for optical payloads. Several techniques have been developed to reduce jitter. One technique is to increase damping of the spacecraft support structure to reduce vibration resp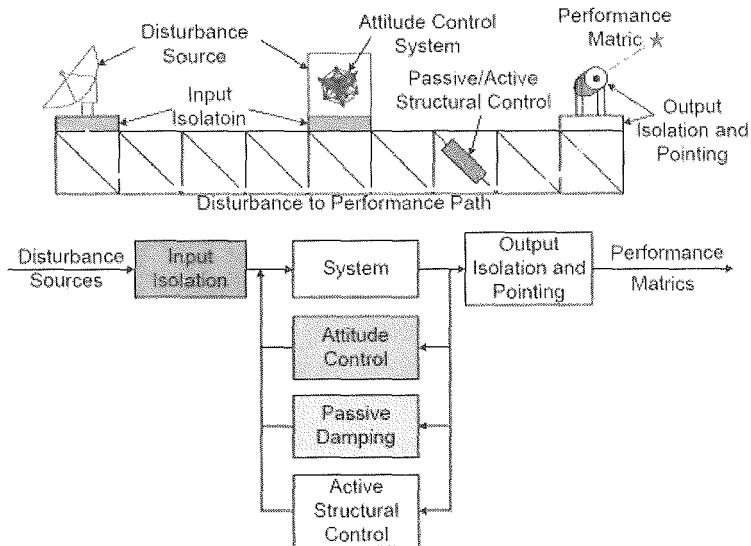onse by adding passive and/or active damping. The second technique is to introduce isolation between vibration source and the spacecraft. The third technique is to isolate the optical payloads from the spacecraft. The fourth technique is to reduce jitter in the optical beam by using a fast steering mirror. Specific problem requires specific, custom solutions. There is no one vibration suppression method that can usually meet all requirements for a certain problem. In general, passive systems perform best for higher frequencies, typically greater than 5 Hz, while active systems perform best for lower frequencies, typically lower than 5 Hz. Most spacecraft jitter control solutions require a hybrid system (passive and active) to suppress the entire range of disturbance frequencies. This paper discusses all these jitter control techniques in the following sections.

Passive Jitter Control

All passive damping treatments share a common goal: absorb significant amounts of strain energy in the modes of interest and dissipate this energy through some energy-dissipation mechanism. The effectiveness of all passive damping methods varies with frequency and temperature, though some more than others. For each of the basic passive damping mechanisms, there are several choices for implementation, which can be divided into two major categories: discrete and distributed.

(a) Free-Layer Treatment   (b) Constrained-Layer Treatment
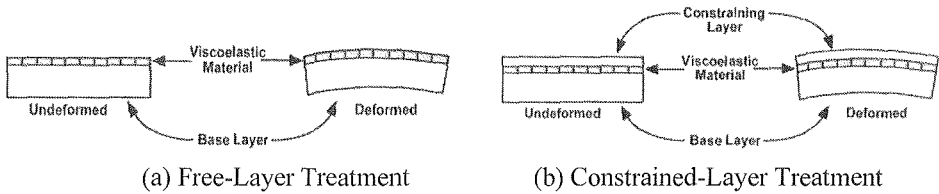
Figure 4. Typical Viscoelastic Material Configuration

For distributed implementation, viscoelastic materials are widely used for damping in both commercial and aerospace applications. Viscoelastic materials are elastomeric materials whose long-chain molecules cause them to convert mechanical energy into heat when they deformed. Figure 4 shows two techniques, free layer treatment and constrained layer treatment. Constraint layer treatment is more effective.

Figure 5. Basic Viscous Fluid Damper

944

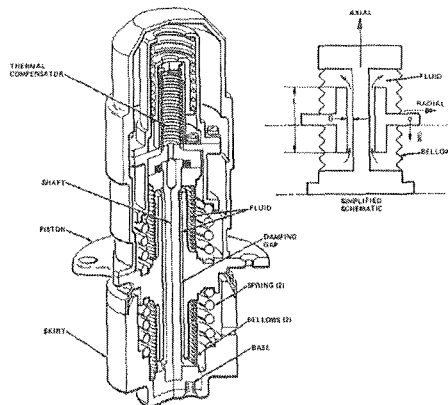For discrete implementation, a viscously damped isolator depicted in Figure 5 is commonly used. Fluid of a specified viscosity is hermetically sealed within two sets of bellows and constrained to flow between them through an orifice when motion occurs. The fluid flow through the orifice provides the damping. A third set of bellows is included to accommodate thermal expansion and contraction of the fluid. Springs are included to provide the desired isolator stiffness. For safety, the device is encased in an outer skirt to protect against contamination from a ruptured bellows. This unit isolator can be simply modeled as a spring in parallel with a spring-damper. By changing the damping (fluid viscosity) of the isolator, the in-band peaking of the isolation characteristic can be changed, but at the cost of isolation bandwidth. Variations in temperature have a similar effect because of its effect on fluid viscosity.

The HST has used passive jitter control methods extensively to meet its telescope-pointing accuracy of 0.007 arc-sec, while suppressing launch vibration for sensitive optical payload. The HST's attitude control system reaction wheels generate low level, high frequency vibration disturbances from imperfections in the electromagnetics and drive electronics, unbalance of the rotor, and imperfections in the spin bearings. The viscous fluid damped isolator for the reaction wheels developed by Honeywell, Inc. is a passive system employing metal springs in parallel with viscous fluid dampers (D-Strut) providing independent, deterministic control of the stiffness and damping characteristics. CSA Engineering developed two methods for launch vibration load suppression: an open/closed cell foam design that provides the required damping and corner frequency attenuation, and a Viscoelastic Material (VEM) design. The flexible solar array panels HST (SA-2) was replaced with greater power generating rigid panels (SA-3) as part of STS Servicing Mission. Analysis of the rigid solar array design shows the HST's pointing control system stability margin will be violated by the new array's fundamental bending modes. CSA Engineering designed and built a damper, integrated into the SA-3 mast, constructed of a titanium flexure and viscoelastic damping material to increase damping of the solar array.
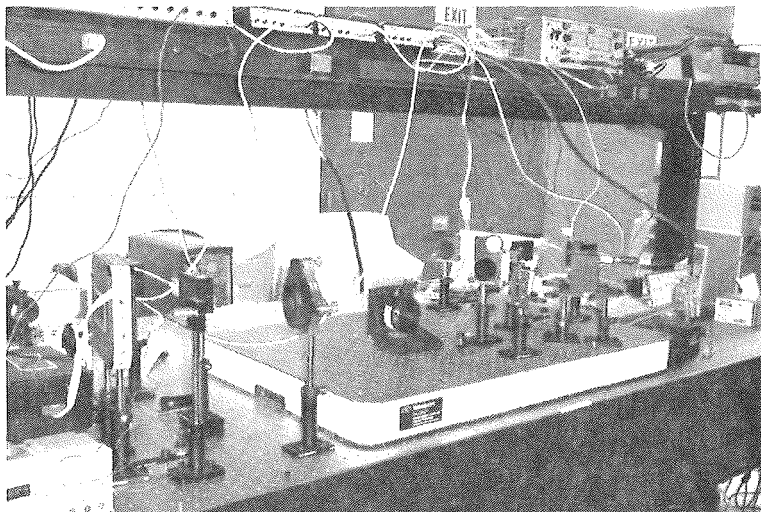
Active Optics Beam Jitter Control

Figure 6. Laser Jitter Control Testbed

To develop improved techniques for optical beam jitter control, a Laser Jitter Control (LJC) testbed was developed at the Naval Postgraduate School (NPS) as shown in Figures 6 and 7. The

945

components are mounted on a Newport optical bench, which can be floated to isolate the components from external vibrations. The laser beam originates from a source and passes through a Disturbance Injection Fast Steering Mirror (DFSM). The DFSM corrupts the beam using random or periodic disturbances, simulating disturbances that might originate with the transmitting station or tip and tilt errors which the beam may suffer as it passes through the atmosphere. A vibration isolation platform is used to mount the relay system and to isolate the relay system from the optical bench. A control Fast Steering Mirror (FSM), designated the CFSM, is used to correct the disturbed beam. The corrected beam is then reflected off the platform to the target Position Sensing Detector (PSD).
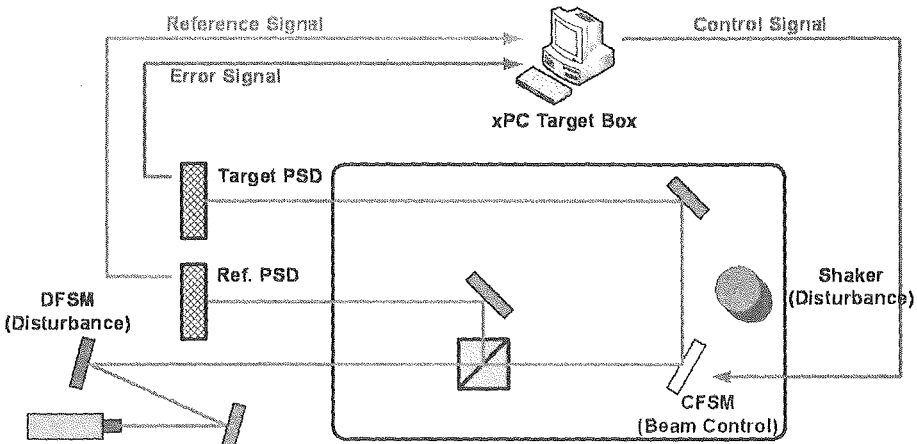

Figure 7. Schematic of the laser jitter control testbed

Laser Jitter Control Using Adaptive Filter

Adaptive filters have been used extensively over the past several decades in the field of active noise and vibration control [4],[5]. The basic principle of an adaptive filter is that controller gains can be varied throughout the control process to adapt to changing parameters and can, therefore, cancel disturbances more effectively than passive methods. Transverse FIR filter structure used for the adaptive filter control method is first described, followed by the weight update algorithms and experimental results

Transverse Filter

An Lth order transverse FIR filter has the structure shown in Figure 8. Each of the L stages, or taps, delays the input signal by one sample, and this filter is sometimes called a tapped-delay line. The filter output is expressed as follows,

$$y(n) = \sum_{i=0}^{L} w_i(n)x(n-i) = w^T(n)x(n) \tag{1}$$

946

where $w(n)$ is the filter weight vector of length L whose i^{th} component is $w_i(n)$, $x(n)$ is the vector of delayed inputs $x(n-i)$, and $y(n)$ is the filter output.
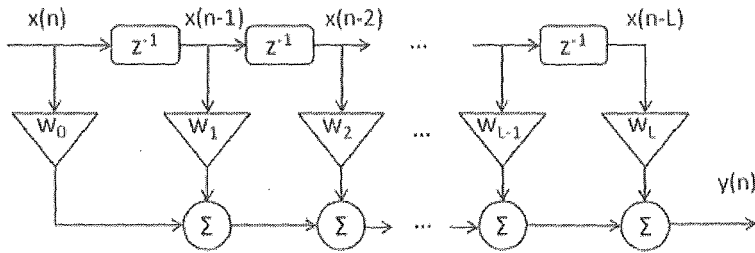

Figure 8. Transverse FIR filter structure

Weight Update Algorithms

Lease Mean Square (LMS) and Recursive Least Square (RLS) are two common algorithms widely used to update the weights. In the LMS algorithm, the cost function $\xi(n)$ is the expectation of $e(n)^2$ called Mean Square Error (MSE) denoted by $E\{e(n)^2\}$. When the statistics of the disturbance and the reference signal are available, the weights that minimize $E\{e(n)^2\}$ can be computed. In practice, however, such a priori information is often unavailable. In LMS algorithm, the MSE is approximated by the instantaneous squared error and iterative steepest-gradient descent method is used to update the weights in the direction toward lowest error. The difference equation for updating weights can be expressed as

$$w(n+1) = w(n) - \frac{\mu}{2}\frac{\partial J[n]}{\partial w(n)} = w(n) + \mu e(n)x(n) \qquad (2)$$

where μ is the convergence coefficient that controls the speed of the convergence to steady-state weight values.

The Recursive Least Squares (RLS) algorithm follows much of the development shown for LMS, with the important exception that it includes past data in its cost function. Instead of expressing the MSE as the instantaneous squared error signal only, the cost function becomes:

$$\xi(n) = \sum_{i=1}^{n} \lambda^{n-i} e^2(i) \qquad (3)$$

where the forgetting factor, $0 < \lambda \leq 1$, allows more recent data to be weighted more heavily and data long past to be forgotten. A value of $\lambda = 1$ implies all previous error history is included in the cost function, while smaller values excludes more past errors. Typical value for λ is [6]

$$1 - \frac{1}{2L} < \lambda < 1 \qquad (4)$$

947

While the error and control signal expressions in RLS are identical to those of LMS, the weight update process is different. Optimal weights could be calculated from the history of all signals in the system if they are available, but keeping all previous history in the digital memory is practically not possible for a long operation of the controller. Instead of calculating and inverting the correlation matrix of the reference input, $R(n)$, the inverse correlation matrix, $Q(n) = R^{-1}(n)$ is calculated recursively. This eliminates the need to the inverse of $R(n)$, greatly reducing the complexity of the RLS algorithm. The recursive equations for weight updates are:

$$z(n) = \lambda^{-1}Q(n-1)x(n) \tag{5}$$

$$k(n) = \frac{z(n)}{z^T(n)z(n)+1} \tag{6}$$

$$w(n+1) = w(n)+k(n)e(n) \tag{7}$$

where $z(n)$ is an intermediate calculation and $k(n)$ is the current gain vector. Finally, the inverse sample correlation matrix is updated as

$$Q(n) = \lambda^{-1}Q(n-1)-k(n)z^T(n) \tag{8}$$

Initial condition of Q is a diagonal matrix whose component is determined by the expected variance of the measurement noise.

$$Q(0) = \frac{1}{\sigma_m^2}\mathbf{I} \tag{9}$$

Filtered-x is a technique to include the effect of the secondary path to avoid potential instability. As shown in Figure 9, the reference signal is passed through a model of the secondary plant, $\hat{S}(z)$ before it is fed to the adaptive algorithm. It can be applied to any weight update algorithms and Filtered-X LMS and RLS adaptive filters are often referred as FXLMS and FXRLS, respectively. In a Filtered-X adaptive filter, the reference signal $x(n)$ in the equations (2) and (5), are replaced by $r(z) = \hat{S}(z)x(z)$, whereas the input of the FIR filter is still $x(n)$ as the output of the filter goes through the actual secondary path.
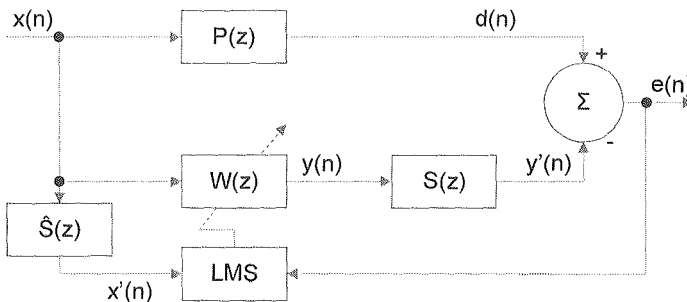

Figure 9. Block Diagram of FXLMS Method

Experimental Results on Active Jitter Control

The experimental mean squared error plot shown in Fig. 10 shows that the FXRLS method manages to further reduce the mean square error of the signal, compared to the FXLMS and LQG designs.
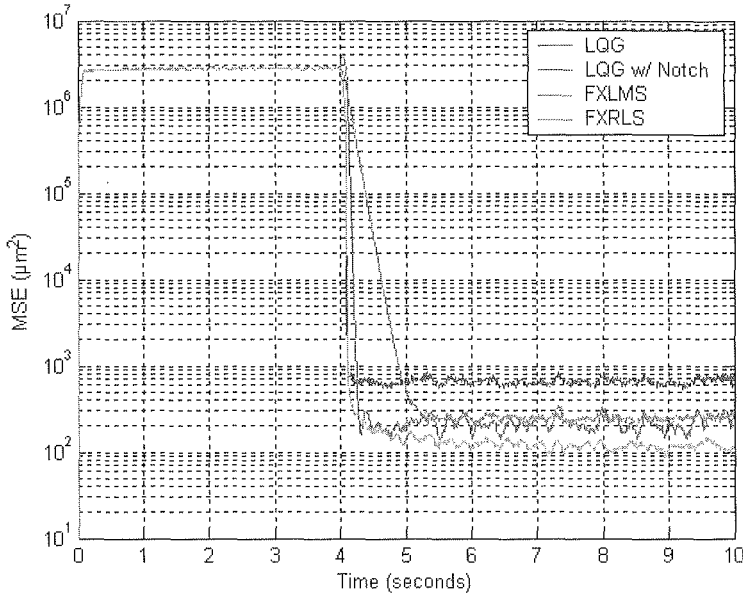

Figure 10. Mean Squared Error for Jitter Control Methods

FLEXIBILITY/CONTROL INTERACTIONS

Imaging spacecraft have several flexible elements such as deployable solar arrays and antennas. Flexibility/control interaction degrades pointing performance and can create instability. For imaging satellites, it is important to minimize this interaction, and increase damping of flexible elements. This area has been studied for many decades. It is common practice to add band-pass and/or notch filters in the control law to provide stability margins. This section gives simple examples on using these filters. Let us consider a rigid body system with the following parameters:

$$\text{Spacecraft Inertia: } J = 65 \text{ kg-m2}$$
$$\text{PID control with } K_p = 17.119, \ K_I = 0.42, \ K_D = 35.285 \tag{10}$$
$$\text{Open loop transfer function: } u_{PID}(s)G(s) = \left(K_p + K_I / s + K_D s\right)\frac{1}{Js^2}$$

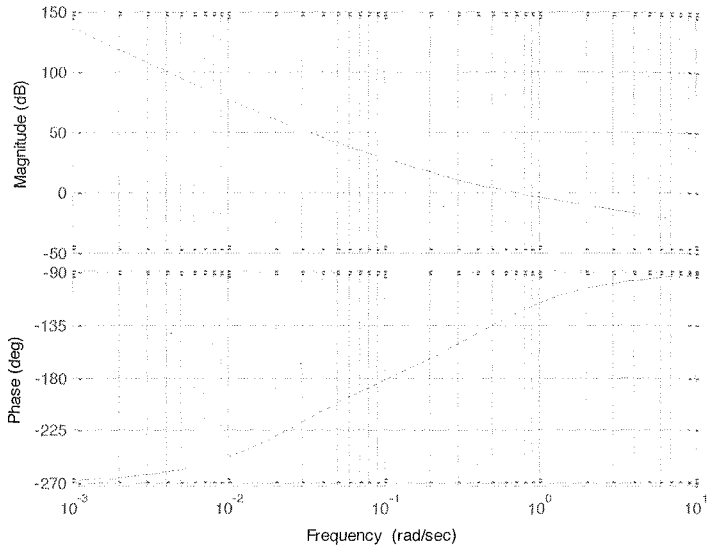With the given control system in Equation 10, the open loop frequency response, Bode diagram, is shown in Figure 11.

Figure 11. Bode Diagram of Rigid Body

This shows that the system has adequate gain and phase margins. If we add flexible appendages, then we will see that there is significant modification to gain and phase diagrams. The gain diagram will have notch at flexible appendage cantilever frequency and peak at spacecraft free-free frequency. Similarly phase diagram goes through 180 degree phase cycle. This can make the system unstable. To make the system stable with adequate margin, band pass and notch filter are commonly used. The transfer functions for these filters are given as follows:

$$\frac{s^2/\omega_z^2 + 2\zeta_z s/\omega_z + 1}{s^2/\omega_p^2 + 2\zeta_p s/\omega_p + 1} \quad \text{with} \quad \begin{array}{l} \omega_z = \omega_c = \omega_p \\ K_{\max} = 20\log_{10}\left(\zeta_z/\zeta_p\right) \end{array} \quad (11)$$

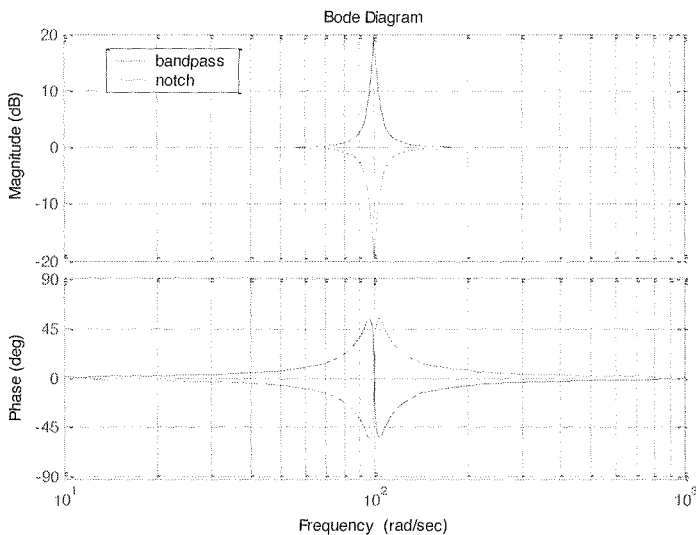The Bode diagram of the filters in Equation 11 is shown in Figure 12.

Figure 12. Bode Diagram of Filters

950

It should be noted that for band-pass filter, $\zeta_z > \zeta_p$, and for notch filter, $\zeta_z < \zeta_p$. Band-pass filters are generally used for flexible cantilever frequencies below cross over frequency and notch filters for free- free frequencies above cross over frequencies.

Figure 13 shows an example open loop Bode diagram where natural frequency is below cross over frequency. In this case band pass filter is used with the following parameters.

$$\omega_c = 0.05, \; \omega_z = 0.05, \; \omega_p = \omega_z$$
$$\zeta_p = 0.001, \; \zeta_z = 0.1$$

(12)

This band-pass filter design avoids the gain crossing zero dB line due to cantilever frequency. The step response plots shown in Figure 14 shows greatly improved flexible control results with the addition of a band pass filter.
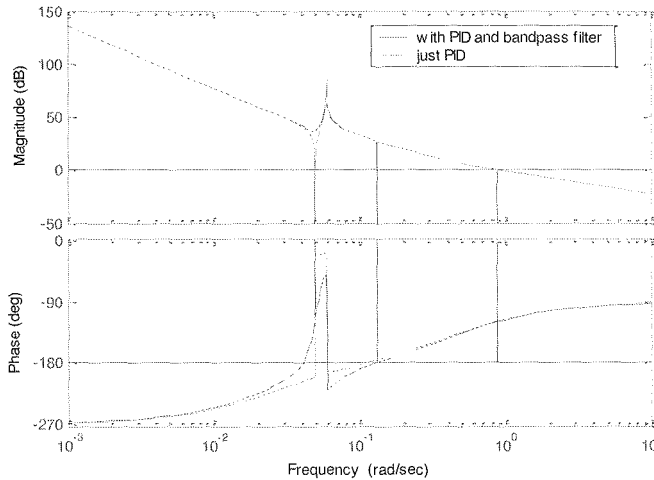

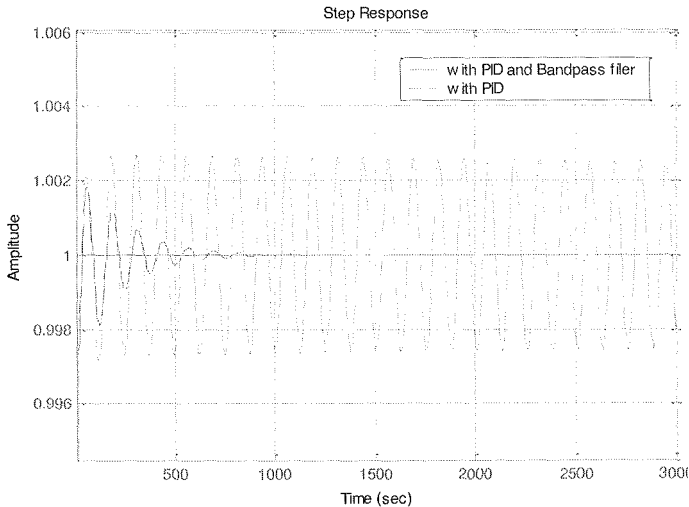**Figure 13. Bode Diagram of Flexible Body**

Figure 14. Step Response of the Flexible System

951

In the next example we add another flexible mode with frequency above the cross over frequency. In this case gain for free-free mode crosses zero dB line. We add notch filter with the following parameters:

$$\omega_c = 3, \ \omega_z = 3, \ \omega_p = \omega_z$$
$$\zeta_p = 0.1, \ \zeta_z = 0.0001,$$

F (13)

Bode diagram and step response with and without notch filter is shown in Figure 16 and Figure 17 with and without a notch filter.
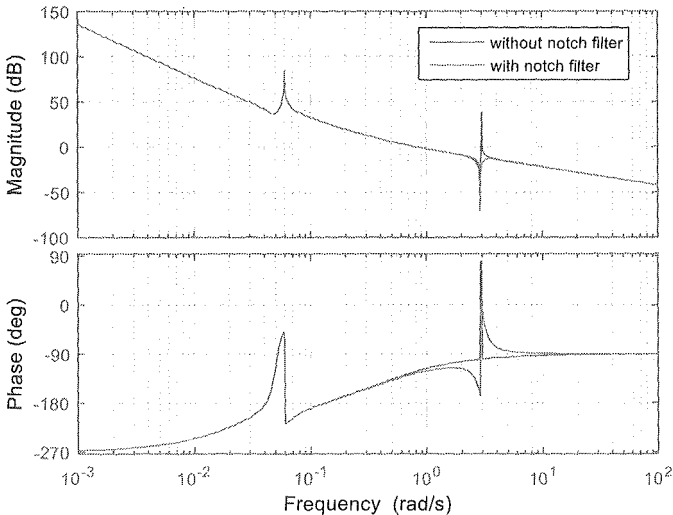

Figure 15. Bode Diagram of Flexible Body with Two Flexible Modes
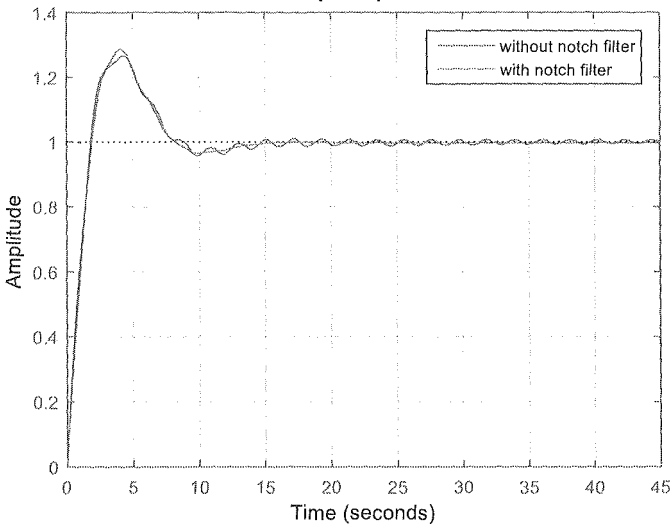

Figure 16. Step Response of Flexible Body with Two Flexible Modes

These examples show how to mitigate flexibility/control interaction problem by using band-pass and or notch filters. It should be noted that in order for these filters to be effective, the natural frequencies of the spacecraft should be known very accurately. Higher damping helps to make the system more stable by reducing peaks or notch due to flexible modes.

SLEW MANEUVERS

Imaging satellites slew from taking pictures from one target to another. At the end of slew due to motion of flexible appendages, it takes some time, called the settling time, before the satellites reach desired pointing. The objective of the research is to evaluate different torque profiles and control techniques for fast slew to minimize settling time. Initially, single axis flexible simulator, as shown in the following figure, was developed at NPS [7] to implement research in this area. Later a three-axis flexible simulator was developed with Control Moment Gyros.
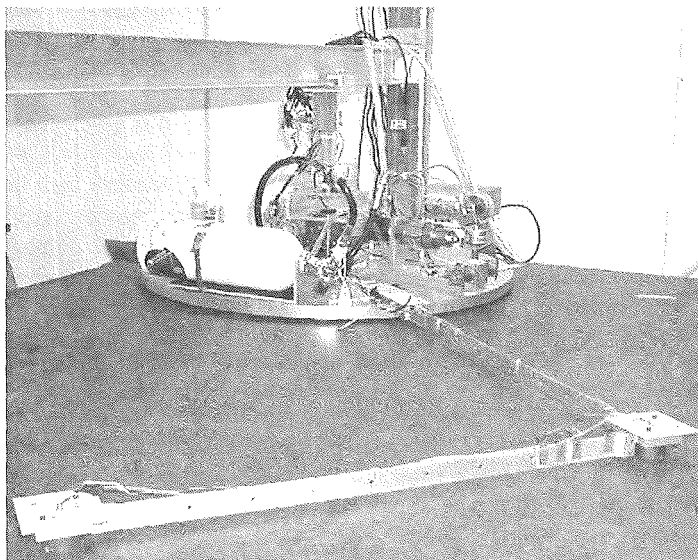

Figure 17. Single Axis Flexible Spacecraft Simulator

The simulator shown in Figure 17 consists of a rigid central body floated on a granite table by air pads. It has an air bearing so that it can rotate in one axis without friction. The central body has a reaction wheel as actuator and an angular sensor and a rate gyro. The center body is connected to L-shaped flexible structure supported on air pads. The torque profile considered in the study are bang-bang, Versine, and input shaping.

Bang-Bang Profile

$$\begin{cases} 1, & 0 \le t \le t_1 \\ -1, & t_1 < t \le t_2 \\ 0, & t_2 < t \end{cases} \tag{14}$$

In bang-bang torque profile, positive maximum torque is applied for half of the period and negative maximum torque is applied for the remaining half of the period. This torque profile provides minimum slew time, however, results in large settling time for flexible spacecraft.
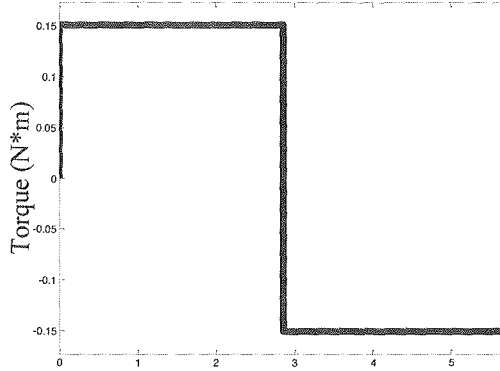

Figure. 18 Bang-Bang Torque Profile

Versine Profile

$$\begin{cases} \frac{1}{2}\left[1 - \cos\left(\frac{\pi t}{t_A}\right)\right], & 0 \le t \le t_A \\ 1, & t_A \le t \le t_B \\ \frac{1}{2}\left[1 - \cos\left(\frac{\pi(t_1 - t)}{t_A}\right)\right], & t_B \le t \le t_1 \\ -\frac{1}{2}\left[1 - \cos\left(\frac{\pi(t - t_1)}{t_A}\right)\right], & t_1 < t \le t_C \\ -1, & t_C \le t \le t_D \\ -\frac{1}{2}\left[1 - \cos\left(\frac{\pi(t_2 - t)}{t_A}\right)\right], & t_D \le t \le t_2 \\ 0, & t_2 < t \end{cases} \tag{15}$$

In the Versine torque profile, sudden change in torque is smoothed using cosine function. This significantly decreases the settling time for flexible spacecraft, but it does, increase the slew time. However, overall slew time is decreased due to lower settling time. This torque profile is commonly used for flexible imaging spacecraft.
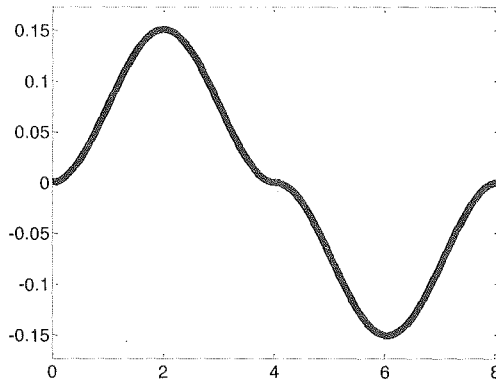
954

Figure 19. Versine Torque Profile

Input Shaping

The goal of input shaping is to provide a command which results in zero residual vibration. As shown in Figure 20, a vibration can be eliminated by applying impulses of appropriate amplitude and phase such that they exactly cancel the vibration mode. For example, the command issued at time t_1, in this case, an impulse, starts a vibration which decays as a function of the modal damping. The second impulse is phased such that it is applied at the vibrating mode's half-period point. The net vibration following the second impulse is zero.
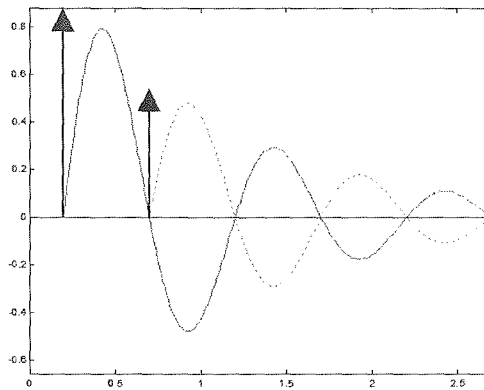

Figure 20. Input Shaping

Torque command is created by convolving a sequence of impulses, an input shaper, with any desired command. The amplitudes and time locations of the impulses are determined by the system natural frequencies and damping ratios.

There are three types of zero vibration (ZV) sequences for the impulses. The shortest impulse train is two impulse ZV sequence. It is robust, however, only small variations (5%) in modal frequency. In order to increase shaper's robustness, we differentiate the vibration equation with re-

spect to natural frequency and it is called Zero Vibration Derivative Shaper (ZVD). It consists of three impulses. It has robustness up to 20% in natural frequency. If the vibration equations are differentiated again, we get Zero Vibration Derivative Derivative Shaper (ZVDD). In this case, we need four impulses. It allows uncertainty up to 40%. Analytical experiments were performed using Versine torque profile and input shaping for one mode and two modes using ZVD.
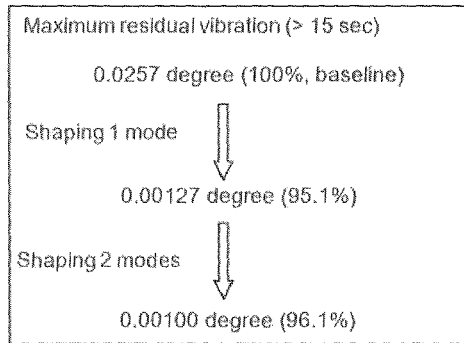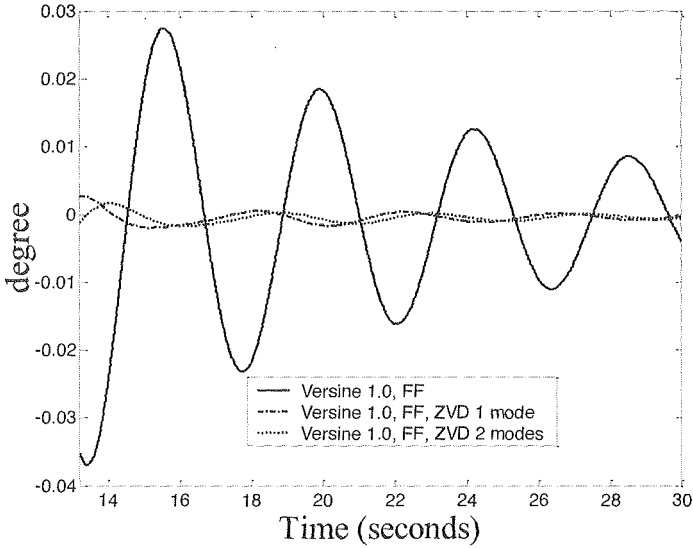
Input Shaping Simulation

Figure 21. Input Shaping Simulation Results for One and Two Modes

Figure 21 shows analytical simulations for input shaping ZVD, maximum vibrations after 15 seconds settling time. Maximum vibrations are reduced by 95.1% for single mode input shaping and 96.1% for two modes input shaping.
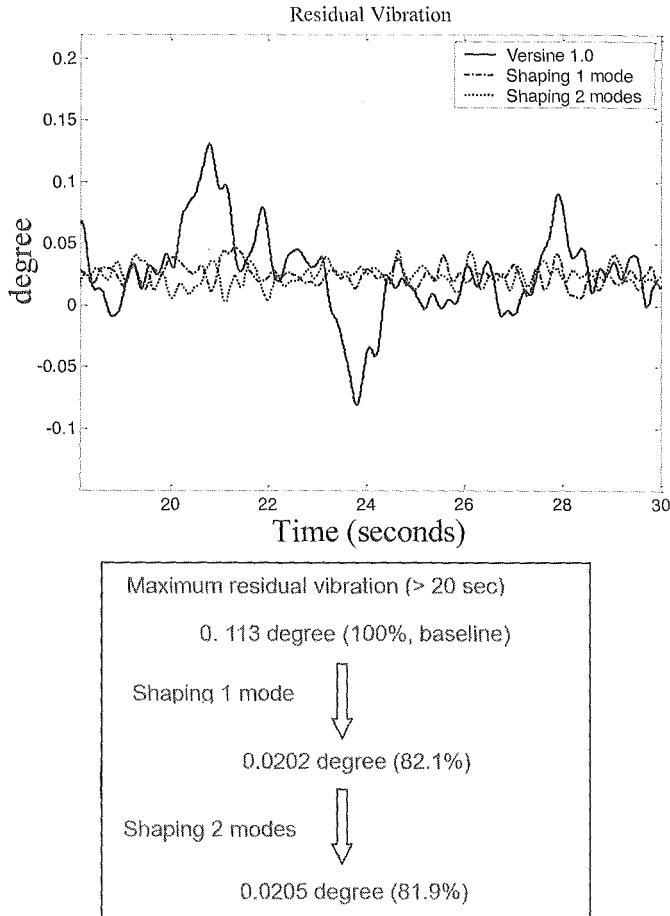
Residual Vibration

Figure 22. Input Shaping Experimental Results for One and Two Modes

Figure 22 shows experimental results for input shaping ZVD, maximum vibrations after 20 seconds. Maximum vibrations are reduced by 82.1% for one mode input shaping and 81.9% for two modes input shaping.

REFLECTOR ACTIVE SURFACE CONTROL

As we have discussed earlier, imaging satellites require surface accuracy, Root-Mean-Square (RMS) surface error, in the range of 0.05 wave in order to get diffraction limited image quality. For visible imaging, it results in 30 nm surface accuracy. It is quite challenging for current imaging satellites as we discussed with HST. In the future, several space imaging missions will need larger space mirrors, 10-20 meters in diameter for improving image resolution or to be used in higher orbit. Due to mass and volume constraints of launch vehicles, these mirrors need to be segmented, light weight, and will be more flexible. Meeting requirements for surface accuracy and alignment

957

for these mirror segments is very challenging. Application of active surface control of reflectors on future spacecraft has the potential to reduce cost and schedule, and higher confidence in meeting on-orbit optical performance. NPS has a 3-meter diameter, six segments incorporating active optics research testbed known as Segmented Mirror Telescope (SMT). The goal of the SMT is to research and develop techniques for actively controlling segment surfaces and their alignments [8], [9].

SMT as shown in Figure 23 consists of six segments. Each segment has 156 face sheet actuators (FSA) for surface control and 3 fine and six coarse actuators for segment alignment. A Shack-Hartman wave front sensor is used for surface control and a phase diversity sensor is used as sensor for segment alignment. A Fast Steering Mirror (FSM) is used for jitter control and field steering.
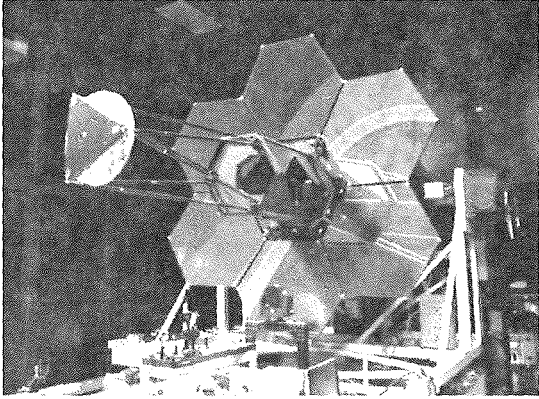

Figure 23. Segmented Mirror Telescope

For optical testing of the SMT, a center of curvature testbed is developed as shown in Figure 24. 4D laser interferometer and the null corrector are mounted on a hexapod for fine alignment of the laser beam. The Null corrector is mounted at center of curvature of the primary mirror which makes the primary mirror function as a spherical mirror. Laser beam from the interferometer passes through the null corrector to the primary mirror. The reflected beam passes back through the null corrector and then into the interferometer. The interferometer measures the wavefront error of the segment surface which is then used to calculate influence coefficient matrix. The influence coefficient matrix is used to develop control laws to drive the face sheet actuators to minimize the surface error present in the segments.
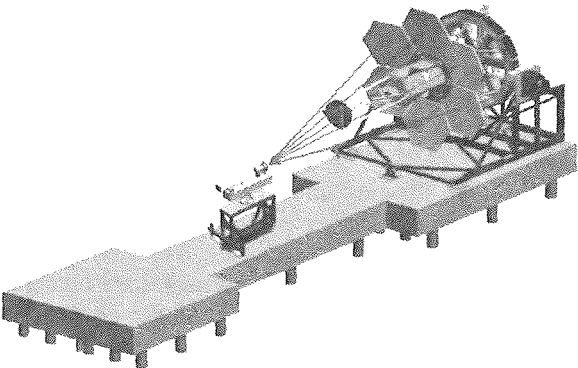

Figure 24. Center of Curvature testbed

958

Influence Coefficient Matrix

The influence coefficient matrix provides a relationship between the actuator input and sensor such as interferometer output and in a linear equation of the form,

$$\{y\} = [\phi]\{u\} \tag{16}$$

in which the actuator input is $\{u\}$, the influence matrix is $[\phi]$, and the sensor output is $\{y\}$. The sensor output, $\{y\}$, provided by the 4D Interferometer is in the form of wavefront phase error at the pixel level. To experimentally determine the influence matrix, a single actuator is commanded at a time. It provides column of the influence matrix. The influence coefficient matrix is given by the following equation.

$$[\phi] = \begin{bmatrix} \phi_{1,1} & \phi_{1,2} & \phi_{1,3} & \phi_{1,4} & \cdots & \phi_{1,n} \\ \phi_{2,1} & \phi_{2,2} & \phi_{2,3} & \phi_{2,4} & \cdots & \phi_{2,n} \\ \phi_{3,1} & \phi_{2,2} & \phi_{3,3} & \phi_{3,4} & \cdots & \phi_{3,n} \\ \phi_{4,1} & \phi_{3,2} & \phi_{4,3} & \phi_{4,4} & \cdots & \phi_{4,n} \\ \vdots & \vdots & \vdots & \vdots & \ddots & \vdots \\ \phi_{m,1} & \phi_{m,2} & \phi_{m,3} & \phi_{m,4} & \cdots & \phi_{m,n} \end{bmatrix} \tag{17}$$

Figure 25 shows influence coefficient matrix with a dimension of 156×156. Different colors represent different values of the phase.
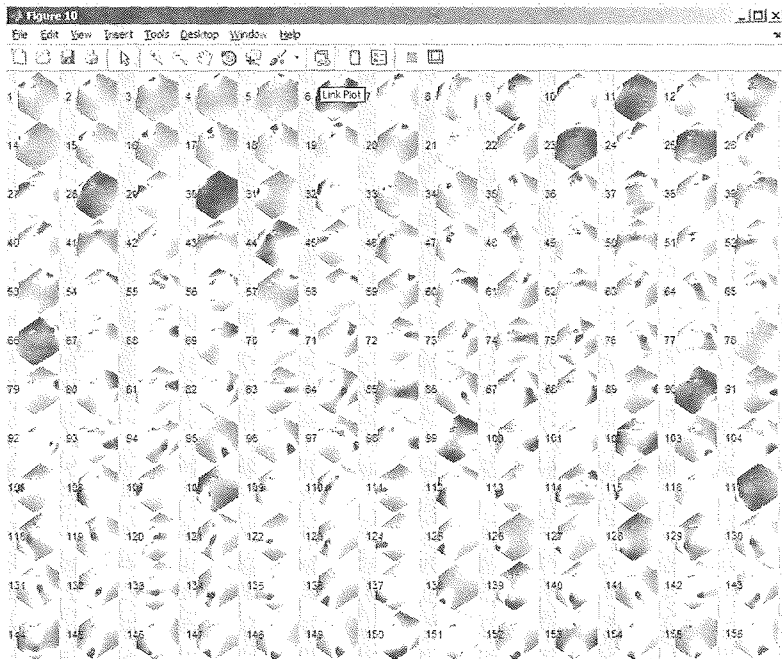

Figure 25. SMT Influence Functions Determined from Experiments

Surface Control Using Unconstrained Least-Squares Solution

After the influence coefficient matrix is determined, the required control is found by solving an unconstrained least square problem utilizing the pseudo-inverse of the influence coefficient matrix, $[\phi]^{\dagger}$

$$\{u\} = [\phi]^{\dagger}\{y\} \tag{12}$$

The unconstrained least square solution is solved in MATLAB with a Moore-Penrose pseudo-inverse that seeks to minimize

$$\min_{x} \frac{1}{2}\left\|[\phi]\{u\} - \{y\}\right\|_2^2 \tag{13}$$

subject to no upper or lower bounds. In order to optimize the solution while remaining within the limits of the available control actuator displacement authority, a solution utilizing constrained least squares curve-fitting optimization is solved of the form;

$$\min_{x} \frac{1}{2}\left\|[\phi]\{u\} - \{y\}\right\|_2^2 \text{ subject to } \{lb\} \leq \{u\} \leq \{ub\} \tag{14}$$

where {lb} and {ub} denotes the lower and upper bound of control respectively.

Constrained optimization was implemented using the lsqlin function in MATLAB. For the present actuators the lower bound is 25V and the upper bound is 75V.
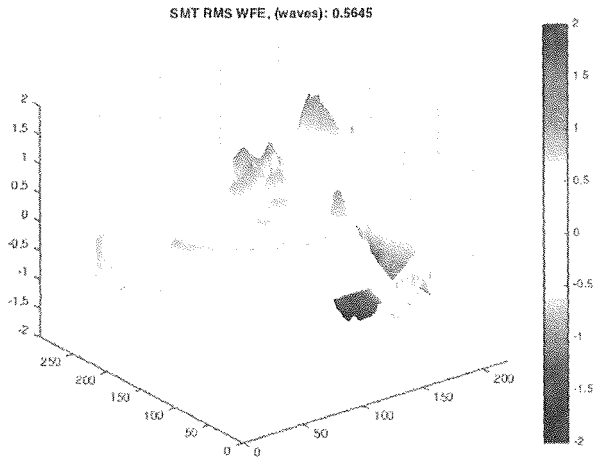

Figure 26. SMT Wavefront Error without Active Surface Control (357 nm RMS)

Figure 26 and Figure 27 show the wavefront errors without actuator control and one with actuator surface control, respectively. Without active surface control, the RMS error of the primary mirror segment is 357 nm or 0.565 waves for a 632.8 nm wavelength beam. After the active surface control is applied, the RMS error reduces to 192 nm or 0.303 waves. It should be noted that wavefront error for SMT surface can be further reduced by increasing the number of actuators.
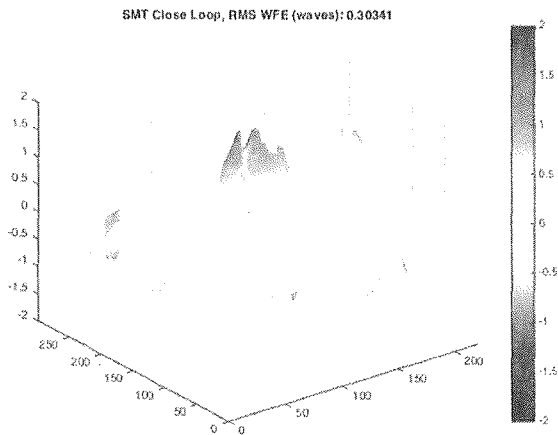
SMT Close Loop, RMS WFE (waves): 0.30341

Figure 27. SMT Wavefront Error with Active Surface Control (192 nm RMS)

CONCLUSION

Imaging satellites have very challenging pointing, jitter control, slewing, flexibility control interaction, and reflector surface accuracy requirements. These requirements provide many challenges in dynamics and control. This paper provides an overview of researches in these areas. In order to meet these requirements, multidisciplinary research efforts are required in advance structural dynamics, control, and optics. These efforts have to be both analytical and experimental demonstration to provide confidence in orbit performance.

Future trends in imaging satellites for large aperture will result in light and deployable reflectors, like James Web Telescope. For these space systems, structural dynamics, control, and active optics become very challenging, requiring development of new techniques to meet pointing, jitter, and reflector surface accuracy requirements.

REFERENCES

[1] https://www.nasa.gov/mission_pages/hubble/story/index.html

[2] https://www.harris.com/solution/james-webb-space-telescope-jwst

[3] Agrawal, B., "Jitter Control for Imaging Spacecraft", proceedings for 4th international conference on Recent Advances in Space Technologies (RAST), 2009, pp 615-620.

[4] Kuo, S. M., & Morgan, D. R., "Active noise control systems", New York: John Wiley & Sons, Inc., 1996.

[5] Watkins, J. R., & Agrawal, B. N. "Use of least mean squares filter in control of optical beam jitter", AIAA Journal of Guidance, Control, and Dynamics, 30(4), 2007.

[6] Hayes, M., "Statistical Digital Signal Processing and Modeling", Wiley, 1996.

[7] Chen, H. and Agrawal, B., "Method of Slewing the Spacecraft to Minimize Settling Time," Paper No. AIAA-2002-4656, AIAA Guidance, Navigation, and Control, Monterey, CA, August 2002.

[8] Agrawal, B. and Kim, J. "Surface Control of Active Hybrid Space Mirrors", Proceedings 65th International Astronautical Congress, Toronto, Canada, IAC-14,C2,5,2,x21485, 2014.

[9] Kim, J., Watson, J., Bagnasco, J., Martinez, T., Fernandez, B., Axtell, T., Wilcox, C., and Agrawal, B., "Correction of Space Telescope Surface Figure Error Using a Deformable Mirror", Proceedings for AIAA SPACE 2014, San Diego, CA, August 2014.